

# Irradiation damage versus lattice distortion in $\text{AlNbTiVCr}_x$ ( $x = 0, 0.5, 1$ ) high-entropy alloys from first-principles calculations and irradiation experiments

Guojia Ge<sup>a</sup>, Feida Chen<sup>a</sup>, Xiaobin Tang<sup>a,b,\*</sup>, Yibo Wang<sup>a</sup>, Changyuan Li<sup>a</sup>

<sup>a</sup> Department of Nuclear Science & Technology, Nanjing University of Aeronautics and Astronautics, Nanjing 211106, China

<sup>b</sup> Key Laboratory of Nuclear Technology Application and Radiation Protection in Astronautics, Ministry of Industry and Information Technology, Nanjing 211106, China

## ARTICLE INFO

### Article history:

Received 19 October 2021

Revised 20 February 2022

Accepted 26 February 2022

Available online 28 February 2022

### Keywords:

High entropy alloys

First-principles calculations

Heavy ion irradiation

Irradiation defects

lattice distortion

## ABSTRACT

Severe lattice distortions and rough energy landscapes were found in low-density, refractory  $\text{AlNbTiVCr}_x$  ( $x = 0, 0.5, 1$ ) high-entropy alloys (HEAs) via first-principles calculations. The corresponding samples were irradiated by 5 MeV Xe ions to fluences of  $3.3 \times 10^{14}$  ions/cm<sup>2</sup> at 600 °C. Fundamental irradiation behaviors were studied using transmission electron microscopy and nanoindentation. No phase decomposition was found after irradiation as well as void. The irradiation-induced dislocation loop size decreases, and the density increases with the increasing Cr content. This finding is attributed to the fact that Cr aggravates lattice distortion and roughens energy landscapes in the  $\text{AlNbTiVCr}_x$  system, which will interrupt the long-distance migration of self-interstitials and delay their accumulation. Nanohardness increments exhibit good consistency with the product of dislocation loop size and density. This work provides an insight into the combination of atomic simulation and irradiation experiments for better understanding of the irradiation behaviors of refractory HEAs, and a possibility to modify defect evolution by regulating the compositional complexity.

© 2022 Elsevier B.V. All rights reserved.

## 1. Introduction

High-entropy alloys (HEAs) have drawn tremendous attention in recent years because of their excellent mechanical properties and irradiation resistance, which originate from unconventional compositions and chemical microstructures [1]. Since HEAs are actually random solid solutions containing multicomponent in near-equiatom proportions [2], they present remarkable local lattice distortions and chemical disorder, thereby providing possibilities to obtain exceptional properties, especially the irradiation resistance. HEAs thus far been explored can be classified into several families, including 3d-transition metal HEAs, refractory metal HEAs and light metal HEAs [1]. The irradiation effects of 3d-transition metal HEAs have been deeply and systematically studied, and the irradiation resistance of 3d-transition metal HEAs can be effectively enhanced through increasing composition complexities [3–6]. The heat dissipation rate during cascade collision process and the defect mobility in the following recovery stage in irradiated HEAs were reduced substantially with the increasing composition com-

plexities. As a result, the recombination time for vacancies and interstitial atoms in HEAs was extended, and the accumulation rate of the defect clusters was sluggish [7]. The unique radiation defect evolution behavior of 3d-transition metal HEAs have stimulated researchers' enthusiasm to explore the application of HEAs to the future advanced nuclear reactors.

However, while advanced nuclear reactor technology has brought sufficient energy conversion efficiency and fuel utilization, it has also increased the operating temperature and neutron energy in reactors, which has driven the demand for materials able to operate under high temperature and extreme irradiation conditions [8,9]. 3d-transition metal HEAs have limited high-temperature performance due to their intrinsic elements' attributes. Refractory HEAs (RHEAs), i.e., HEAs based on refractory elements, are good for thermally harsh environment applications. The locally disordered chemical environment in RHEAs is also expected to cause irradiation- and corrosion-resistant properties [10–12]. However, RHEAs that were initially developed had the disadvantage of high density of more than 10000 kg·m<sup>-3</sup>. Recently, studies suggested that the addition of light element in RHEAs has beneficial effects on density and strength [13–15]. For example, the  $\text{AlNbTiV}$  alloy has low density of 5590 kg·m<sup>-3</sup>, single body-centered cubic (BCC) phase structure, and yield strength of 1020 and 685 MPa

\* Corresponding author.

E-mail address: [tangxiaobin@nuaa.edu.cn](mailto:tangxiaobin@nuaa.edu.cn) (X. Tang).

at room temperature and 800 °C, respectively, outperforming currently used Ni-based superalloy [16]. Moreover, the high temperature strength of the AlNbTiV can be further improved through the introduction of Cr without significantly increase in density ( $< 5900 \text{ kg}\cdot\text{m}^{-3}$ ) [17]. This design strategy greatly enhances the flexibility of RHEAs for application in advanced nuclear energy systems, especially for space nuclear reactors. The high strength (high temperature) and density ratios enable the low-density RHEAs to satisfy the requirements of complex service environments. However, knowledge about the irradiation resistance of such alloys is limited.

We focused on the microstructure and defect migration behavior of Al-Nb-Ti-V-Cr<sub>x</sub> ( $x = 0, 0.5, 1$ ) alloy system at the atomic scale to achieve a better understanding on fundamental irradiation effects of low-density RHEAs. AlNbTiVCr<sub>x</sub> system with varying concentrations of Cr was selected because (i) it has the remarkable high temperature strength with low density as mentioned above; (ii) The irradiation effects of Cr in face-centered cubic alloys have been widely discussed, it was found that Cr affects the dislocation loops as a strengthening mechanism in many aspects [18–20], e.g. Cr decreases the mobility of small dislocation loops. It is worthy to study the role of Cr in irradiated BCC HEAs. First-principles calculations were employed to reveal the lattice distortion and defect energy of AlNbTiVCr<sub>x</sub> alloys. The results showed that Cr aggravates the lattice distortion and roughens the energy landscapes. Phase stability, structural damage, and mechanical changes of AlNbTiVCr<sub>x</sub> alloys were also characterized after ion irradiation experiments. The simulation and experiments results showed a good agreement.

## 2. Methods

### 2.1. First-principles calculations

The chemical disorder of the AlNbTiVCr<sub>x</sub> ( $x = 0, 0.5, 1$ ) alloys was modelled as special quasirandom structures (SQS) [21] generated by the *mcsqs* code of the ATAT package [22]. Their correlation functions match perfectly with the corresponding ideal random alloys for the first nearest neighbors [23]. Supercells of 128-atom were generated for three alloy compositions in a  $4 \times 4 \times 4$  BCC lattice. Calculations were carried out with the projector augmented wave (PAW) method and Perdew–Burke–Ernzerhof (PBE) functional [24] for exchange-correlation potential implemented in Vienna *Ab-initio* Simulation Package (VASP) codes [25,26]. The irreducible Brillouin zone was sampled with a Gamma-centered  $3 \times 3 \times 3$  k-mesh for all calculations. The relaxation of the electronic degrees of freedom was achieved when the change in the total energy was smaller than  $10^{-4}$  eV/cell. The optimized atomic geometry was achieved through minimizing Hellmann–Feynman forces acting on each atom until the maximum forces on the ions were smaller than 0.01 eV/Å.

The defect formation energy is calculated as follows [27,28]:

$$E_f = E_d - E_0 \pm \mu_d, \quad (1)$$

where  $E_d$  and  $E_0$  are the energies of supercells with or without defect, respectively, and  $\mu_d$  is the chemical potential of defect species added to or removed from the perfect lattice to create the defect, which corresponds to the signs of + and -. Chemical potentials were obtained from Widom-type substitution techniques [29], as follows:

$$\mu_A - \mu_B = E^{A \rightarrow B} - E_0, \quad (2)$$

$$E_0 = N_A \mu_A + N_B \mu_B, \quad (3)$$

where  $E^{A \rightarrow B}$  is the total energy of the alloy with one B atom substituted by A.  $N_A$  and  $N_B$  are the numbers of A and B atoms in

a perfect lattice, respectively. A set of element substitutions was considered, and the energy differences were calculated. Then, the chemical potential of different elements can be solved by the combination of Eqs. (2) and (3).

### 2.2. Experiment procedures

The alloys with nominal composition of 25%Al-25%Nb-25%Ti-25%V, 22%Al-22%Nb-22%Ti-22%V-12%Cr, and 20%Al-20%Nb-20%Ti-20%V-20%Cr, further denoted as AlNbTiV, AlNbTiVCr<sub>0.5</sub>, and AlNbTiVCr, were produced by vacuum-levitation, melting a mixture of pure metals in a low-pressure, and high-purity argon atmosphere inside a water-cooled copper cavity. The source materials had a purity level higher than 99.9 wt.%. To ensure chemical homogeneity, the ingots were flipped over and re-melted at least four times. The structure of the as-fabricated samples was characterized by conventional X-ray diffraction (XRD) measurements (Rigaku Ultima IV with Cu K-alpha radiation) operated at 40 kV voltage, 40 mA current, and 0.02 step size.

Ion irradiations were performed at the Institute of Modern Physics, Chinese Academy of Sciences (CAS). AlNbTiVCr<sub>x</sub> ( $x = 0, 0.5, 1$ ) samples were irradiated with 5 MeV Xe ions to fluences of  $3.3 \times 10^{14}$  ions/cm<sup>2</sup> at 600 °C. The damage profiles were calculated by the Stopping and Range of Ions in Matter-2013 (SRIM) software in Quick Kinchin–Pease mode with a displacement threshold energy of 25, 60, 30, 40, and 40 eV for Al, Nb, Ti, V, and Cr, respectively [30]. The result of the damage caused by above irradiation condition is approximately 1 dpa at the damage peak.

The microstructural damage and phase stability of irradiation specimens were characterized by cross-section transmission electron microscopy (TEM) (FEI Talos F200X operated at 200 kV). TEM specimens from the irradiated samples were prepared using a focus ion beam (FIB) system with Ga<sup>+</sup> ions. The ion energy at the main thinning step was 30 keV, and during the later stages of thinning, the energy was progressively reduced to 5 and 2 keV to remove the ion-induced surface amorphous layer and reduce the damage caused by the FIB process.

The irradiation-induced mechanical change was characterized by nanoindentation tests (Nano Indenter G200, Agilent). All the tests were performed in continuous stiffness measurement (CSM) with a Berkovich-type indenter [31]. Five indents were made for each depth with 100 μm spacing between two indents to avoid any overlap of their plastic zones. Nanohardness was measured as a function of depth from the point of contact of the nanoindenter with the surface to a depth of approximately 1600 nm. The hardness data within 120 nm from the sample surface was discarded due to large data scatter associated with surface roughness. A method proposed by Kasada based on the Nix–Gao model was applied to extract the actual hardness data of damaged areas by fitting curves [32,33]. Nanohardness can be obtained from the following:

$$H = H_0 \sqrt{1 + \frac{h^*}{h}}, \quad (4)$$

where  $H_0$  is the hardness at infinite depth;  $h$  is the indentation depth of the indenter, and  $h^*$  is a characteristic length that depends on the shape of the indenter tip and the type of material.

## 3. Results

### 3.1. Lattice distortion

In order to better understand the local lattice distortion of the AlNbTiVCr<sub>x</sub> ( $x = 0, 0.5, 1$ ) alloys, the distributions of the first and second nearest neighbor (NN) distances in the three alloy models after a full relaxation are shown in Fig. 1. Both the 1NN and 2NN

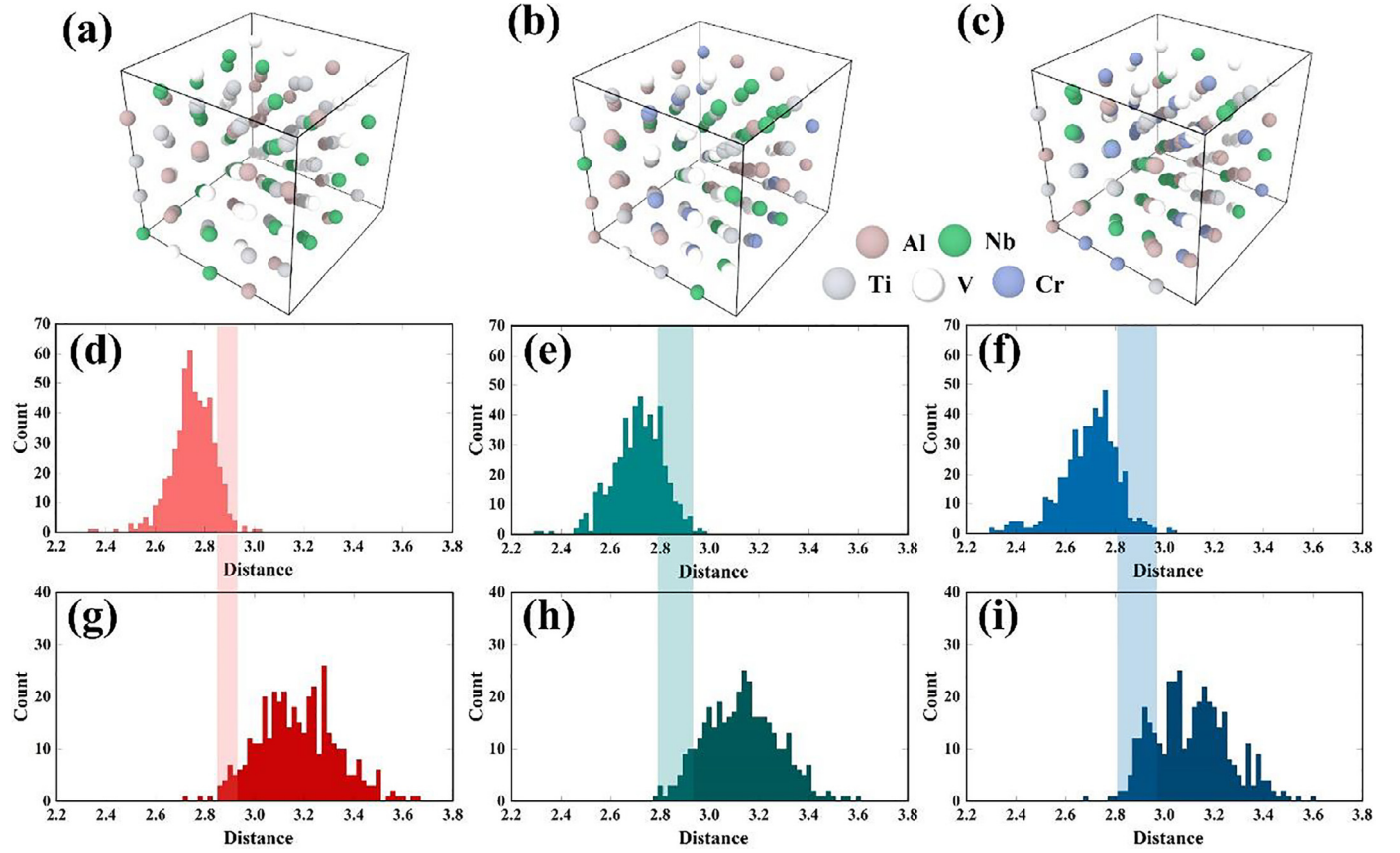


**Fig. 1.** Atom structure (a–c) and distribution of the interatomic distances for the (d–f) 1NN and (g–i) 2NN in (a, d, g) AINbTiV, (b, e, h) AINbTiVCr<sub>0.5</sub>, and (c, f, i) AINbTiVCr alloys after a full relaxation from first-principles calculation. The rectangle shows the overlap region of 1NN and 2NN.

distance extends over a wide range, suggesting that atoms deviate profoundly from their ideal lattice site, leading to a notable local lattice distortion in this alloy system [34]. Moreover, it was found three characteristics of the NN distribution changed with the increase in Cr content, as follows: (i) the integral distribution of 1NN shifts to a smaller value; (ii) the 1NN distribution extends to a wider range; (iii) the distribution of 1NN and 2NN shows an overlap region and increases. The former associates with the small atomic size of Cr, and the two other characteristics indicate greater local lattice distortion introduced by Cr.

To quantitatively compare the lattice distortion of the three studied alloys, we refer to the calculation of atomic radius mismatch and introduce the parameter  $\delta_{1NN}$  in term of 1NN distance, which can be obtained from the following:

$$\delta_{1NN} = \sqrt{\sum_i^n \frac{1}{n} \left(1 - \frac{d_{1NN}^i}{\bar{d}_{1NN}}\right)^2}, \quad \bar{d}_{1NN} = \frac{\sum_i^n d_{1NN}^i}{n}, \quad (5)$$

where  $n$  is the total count of 1NN in the studied alloy;  $d_{1NN}^i$  is the distance of the  $i$ th 1NN. The average 1NN distances and  $\delta_{1NN}$  are listed in Table 1. The values of  $\delta_{1NN}$  increase with the increasing Cr content, indicating an aggravated lattice distortion effect. The contribution of each element in AINbTiVCr to lattice distortion were

further explored in term of the average displacement and average partial density of states (PDOS) of  $d$  orbitals, and the results are given in Fig. 2. The displacement distances do not follow the trend of atomic size but have strong correlation with the DOS values. Large DOS value near the Fermi energy indicates the lattice instability and require large relaxation distance [35]. Thus, Cr and V exhibit larger displacement than Nb and Ti to stabilize the lattice in AINbTiVCr.

### 3.2. Interstitial energetics

The lattice distortion largely influences the defect energetics. The formation energy of interstitials was calculated in the relaxed 54-atom AINbTiVCr<sub>0.5</sub> model. Ten octahedral sites with different local chemical environment and five types of elements were considered. The total of fifty calculations shows that all the interstitials form dumbbell interstitials along the [111] direction, as shown in Fig. 3. 64% interstitials combine with Cr atom to form Cr-X (X = Al, Nb, Ti, V, Cr) dumbbells, 32% form the V-X dumbbells, and the rest are dumbbells without Cr or V. This factor may also attribute to the large DOS value of Cr and V. Since Cr has the highest peak value among the five elements and V come second. Interstitials prefer to combine with Cr atom to stabilize the lattice and reduce the energy of the system.

The elemental chemical potentials and interstitial formation energies in AINbTiVCr<sub>0.5</sub> are listed in Table 2. The values of formation energy are much lower than those in other HEAs, but consistent with the result that Cr-Cr and V-Cr exhibit the lowest formation energies among the stable interstitial dumbbells studied in VTaCrW alloy [35]. The lowest Cr interstitial formation energy also agrees with the interstitial structure exhibited in the

**Table 1**  
Average 1NN distances and  $\delta_{1NN}$  in AINbTiVCr.

System	$\bar{d}_{1NN}$ (Å)	$\delta_{1NN}$
AINbTiV	2.7610±0.0847	0.0307
AINbTiVCr <sub>0.5</sub>	2.7217±0.1012	0.0372
AINbTiVCr	2.7048±0.1163	0.0429

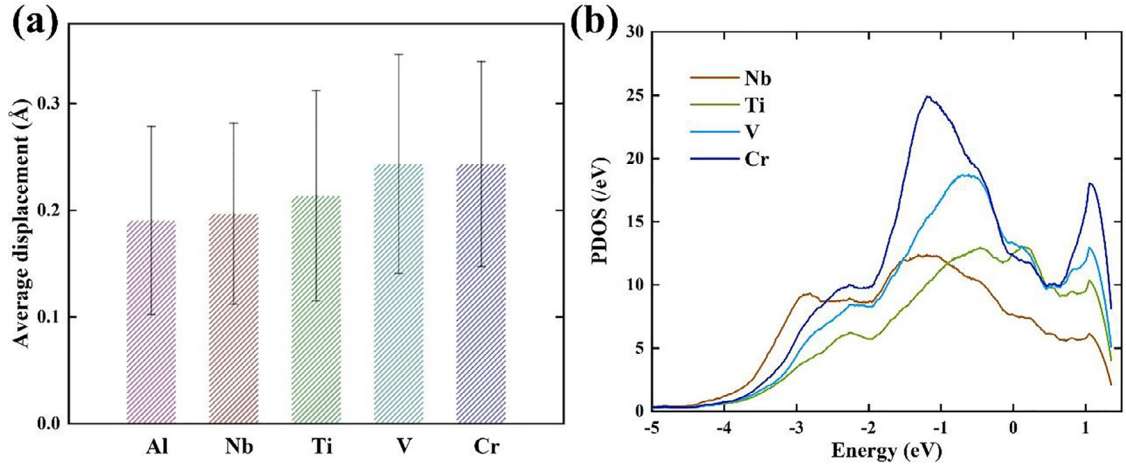


**Fig. 2.** (a) Average displacement of each element in AlNbTiVCr; (b) Average partial density of states (PDOS) of *d* orbitals for Nb, Ti, V and Cr in AlNbTiVCr.

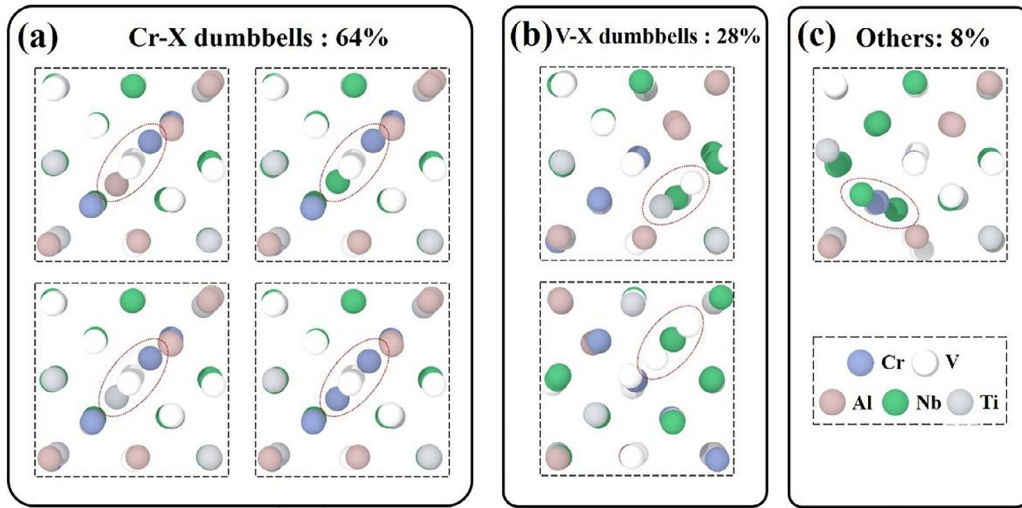


**Fig. 3.** Stable interstitial structures after full relaxation. (a) for the Cr-X dumbbells, (b) for the V-X dumbbells, and (c) for the dumbbells without Cr or V. The formation probabilities of each type of dumbbell are included.

**Table 2**  
Elemental chemical potentials and interstitial formation energies of different elements in AlNbTiVCr<sub>0.5</sub>.

Element	$\mu$ (eV/atom)	$E_f$ (eV)
Al	-4.37	2.31±0.49
Nb	-9.92	2.14±0.42
Ti	-7.85	2.22±0.48
V	-8.87	1.90±0.56
Cr	-9.17	1.46±0.47

studied alloy. In concentrated alloys, the chemically biased diffusion is the main mechanism for mass transport under ion irradiation [36,37]. The calculations show that Cr greatly affects the energy landscapes and microstructures of the studied alloys, which will modify energy and mass transport on their irradiation response.

### 3.3. Phase stability

The phase structures of the as-fabricated and irradiated AlNbTiVCr<sub>x</sub> ( $x = 0, 0.5, 1$ ) alloys are presented in Fig. 4. Fig. 4(a) shows the XRD patterns of the three as-fabricated alloys, and all the Bragg peaks belong to a single phase with a BCC crystal structure. The two strong diffraction peaks possibly due to strong crys-

tallographic texture of the AlNbTiV alloy agree with Stepanov's study [17]. The peaks of AlNbTiVCr<sub>0.5</sub> shift to lower  $2\theta$  than AlNbTiV, indicating a decreased lattice constant, which is consistent with the small atomic size of Cr. However, different from the previous work that Laves phase was formed in the AlNbTiVCr<sub>0.5</sub> and AlNbTiVCr alloys [17,38], no second phase was found in this study. The reason can be explained by the rapid cooling rate inside a water-cooled copper cavity during the casting process; thus, the equilibrium state cannot be achieved. Therefore, the as-fabricated samples have much simpler structure than the equilibrium phase diagram prediction [17]. The absence of Laves phase in the studied alloys is beneficial for reactor application [39]. In addition, the same single-phase structure of the three alloys enables us to focus on the effect of Cr content on the irradiation behavior without the confounding effects of the secondary phases.

Figs. 4(b–g) show the selected area electron diffraction (SAED) pattern of irradiated region (b–d) and unirradiated (e–g) region of the AlNbTiVCr<sub>x</sub> alloys at 600 °C, taken from the (b, e) [111], (c, d, f, g) [011] zone axis, respectively. Only diffraction spots belonging to the BCC structure are observed, indicating a high phase stability against irradiation and high temperature. The phase stability of the studied alloys is attribute to the HEAs' core effects, including high-entropy effect and sluggish diffusion effect, interfere with complex-phase formation and slow down phase



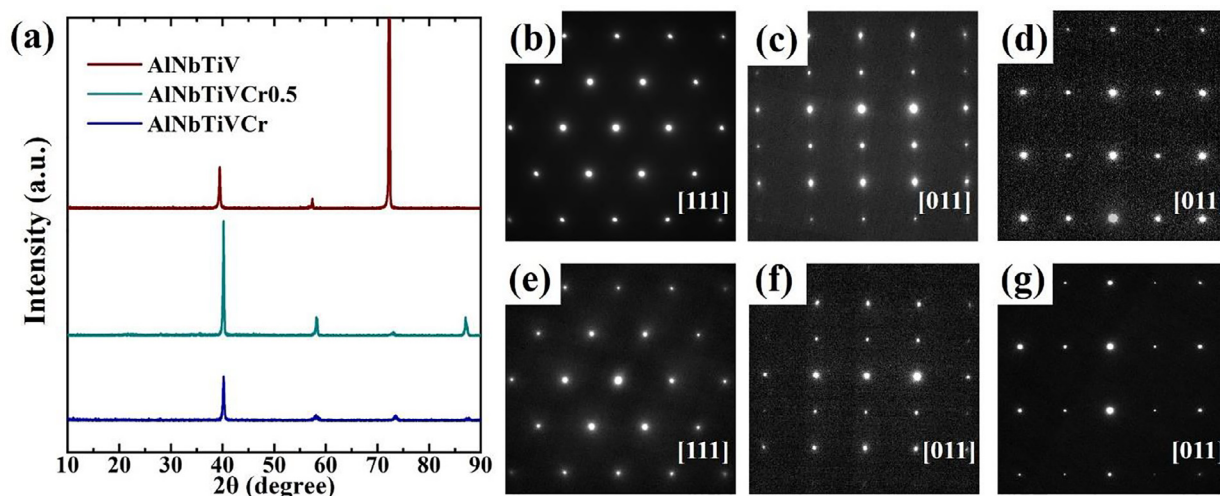


**Fig. 4.** (a) XRD patterns from the as-fabricated  $\text{AlNbTiVCr}_x$  ( $x = 0, 0.5, 1$ ) alloys. Selected area electron diffraction (SAED) patterns of irradiated region (b–d) and unirradiated (e–g) region of the (b, e)  $\text{AlNbTiV}$ , (c, f)  $\text{AlNbTiVCr}_{0.5}$ , and (d, g)  $\text{AlNbTiVCr}$  alloys irradiated at 600 °C to 1 dpa, taken from the (b, e) [111], (c, d, f, g) [011] zone axis, respectively.

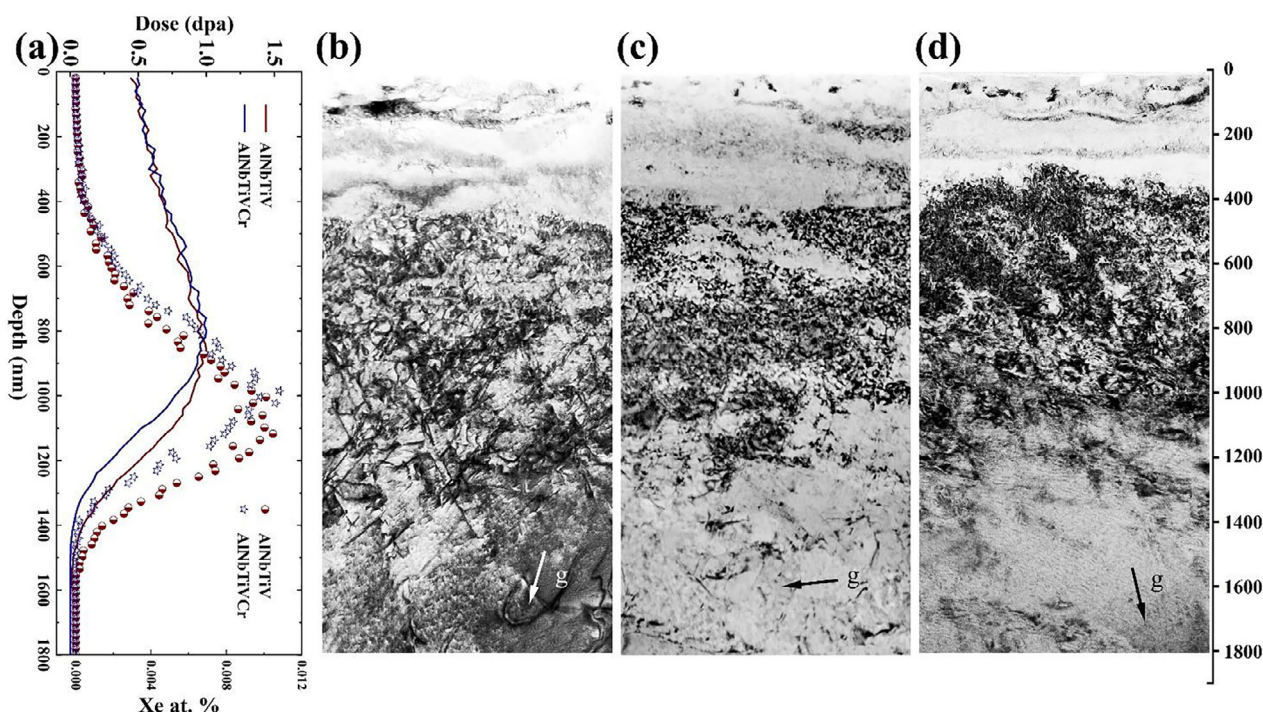


**Fig. 5.** (a) SRIM-calculated damage profiles and Xe distribution of  $\text{AlNbTiV}$  and  $\text{AlNbTiVCr}$  irradiated with 5 MeV Xe ions to fluences of  $3.3 \times 10^{14}$  ions/cm<sup>2</sup>; (b–d) cross-sectional TEM images of the (b)  $\text{AlNbTiV}$ , (c)  $\text{AlNbTiVCr}_{0.5}$ , and (d)  $\text{AlNbTiVCr}$  alloys irradiated at 600 °C. All micrographs were taken under two-beam BF conditions using a diffraction vector  $g = 110$ .

transformation. In addition, the high intrinsic interatomic stress associated with large lattice distortion renders the  $\text{AlNbTiVCr}_x$  alloys to easily experience amorphization-recrystallization process under irradiation [40,41], which is beneficial to the phase stability against irradiation.

### 3.4. Irradiation-induced dislocation loops

Fig. 5 shows the cross-sectional TEM images of  $\text{AlNbTiVCr}_x$  ( $x = 0, 0.5, 1$ ) alloys irradiated by 5 MeV Xe ions to 1 dpa at 600 °C. All micrographs were taken under two-beam kinematical bright-field (BF) conditions using a diffraction vector  $g = 110$ , and the zone axis is [111], [011], and [011] for  $\text{AlNbTiV}$ ,  $\text{AlNbTiVCr}_{0.5}$ ,

and  $\text{AlNbTiVCr}$ , respectively. The SRIM-calculated damage profiles and Xe distribution of  $\text{AlNbTiV}$  and  $\text{AlNbTiVCr}$  are also included. No void is found in the three alloys. Meanwhile, the distribution and morphology of dislocation defects are varied with the increase of Cr content. In  $\text{AlNbTiV}$  (Fig. 5(b)), the dislocation structures mostly distribute over the depth of 800–1400 nm, cover the second half of the SRIM predicted radiation damaged profile. Instead, the dislocation structures in  $\text{AlNbTiVCr}$  (Fig. 5(d)) concentrate on the predicted peak damage region. And the defect morphologies are more like "black dots" or tiny dislocation loops with high density. The dislocation loop distribution and morphology in  $\text{AlNbTiVCr}_{0.5}$  (Fig. 5(c)) are assumed to be the transition state between the two alloys.

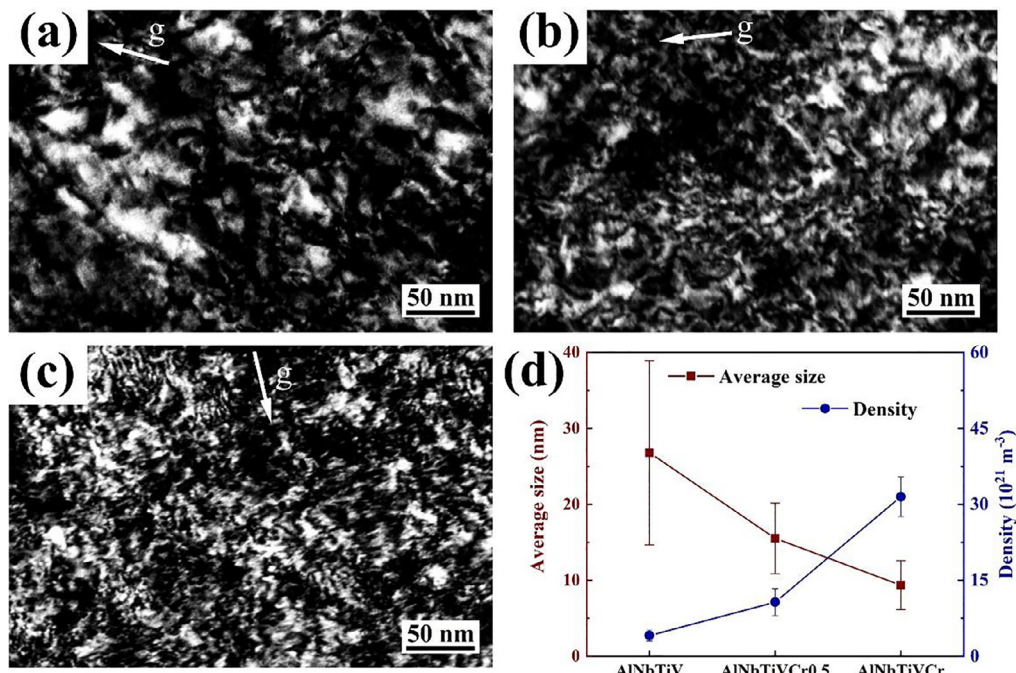


**Fig. 6.** (a)–(c) Characterization of dislocation in (a) AlNbTiV, (b) AlNbTiVCr<sub>0.5</sub>, and (c) AlNbTiVCr alloys irradiated at 600 °C to 1 dpa under DF conditions ( $g = 110$ ); (d) Average size and density of the dislocation loops.

Detailed characterization of dislocation in three samples under dark-field (DF) conditions is shown in Fig. 6, the diffraction vector and the zone axis are the same as the previous BF conditions. The statistic average size and density of dislocation are also included. It can be seen that the size monotonically decreases, and the density monotonically increases with the increasing Cr content. The average loop size in AlNbTiVCr reached 9.34 nm, which is much smaller than the loop size in 316 steels at the same or close irradiation temperature [42–44]. The small size and high density of loops in AlNbTiVCr suggests that the long-distance travel of self-interstitials are interrupted. Williams [43] reported that the loop size in 1 dpa Ni ion-irradiated 316 stainless steel increased from ~5 nm at 400 °C to ~30 nm at 600 °C. In this study, loop size increased from ~9 nm in AlNbTiVCr to ~27 nm in AlNbTiV. And the loop density in the three studied alloys has similar trend to the stainless steels or other HEAs, where the loop density decreases with the increase in irradiation temperature [44–46]. The qualitatively similar evolution of irradiation-induced defects with compositional complexity and with temperature implies that compositional complexity significantly changes the defect diffusion kinetics.

### 3.5. Irradiation-induced hardening

Fig. 7(a–c) shows the depth-dependent hardness values of the pristine and irradiated AlNbTiVCr<sub>x</sub> ( $x = 0, 0.5, 1$ ) alloys. The nanohardness data plotted as the square of the hardness ( $H^2$ ) versus the reciprocal of the indentation depth ( $1/h$ ) are presented in Fig. 7(d–f). The hardness of pristine samples increases as the Cr content increases, indicating a crucial role of solid solution strengthening effect by Cr. The presence of irradiation defect clusters, such as dislocation loops, increases the hardness by acting as obstacles to the glide of dislocations. The AlNbTiV and AlNbTiVCr<sub>0.5</sub> present a certain degree of irradiation-induced hardening. But the hardness of the irradiated AlNbTiVCr decreases as shown in Fig. 7 (c). We speculate that this is due to the softening caused by 600°C heating process during irradiation. The high intrinsic interatomic stress associated with large lattice distortion

in the AlNbTiVCr may be released to some extent after heat treatment. Since its intrinsic hardness is the highest among the three studied alloys, and is much higher than that of traditional stainless steel, the decrease of hardness is relatively more significant. However, irradiation-induced hardening still occurred in the irradiated AlNbTiVCr. Because the curve of the irradiated sample in Fig. 5(f) has an inflection at a critical indentation depth of ~300 nm. The inflection point divided the curve into two linear parts. The left linear part is the result of the soft substrate effect (SSE) [47,48]. Specifically, the hemispheric influence zone of indenter can reach 4–10 times the indentation depth, that is, SSE in unirradiated region can contribute to the hardness from increasing the indentation depth [49]. The right linear part is the result of irradiation-induced hardening. The result showed that the slope change of the bilinear of AlNbTiV and AlNbTiVCr<sub>0.5</sub> is modest and comparable. While the AlNbTiVCr has a rapid decline in slope, corresponding to a significant hardening effect.

The contribution of irradiation-induced defects on hardening has a strong correlation with the defect size and density, which can be interpreted by the dispersed barrier-hardening (DBH) model [50], as follows:

$$\Delta\sigma_y = M\alpha\mu b\sqrt{Nd}, \quad (6)$$

where  $\Delta\sigma_y$  is the increase in yield strength;  $M$  is the Taylor factor (3.06 for equiaxed BCC metals);  $\alpha$  is the defect barrier strength (~0.4 for dislocation loops);  $\mu$  is the shear modulus;  $b$  is the Burgers vector of gliding dislocations;  $N$  and  $d$  are the number densities and diameter of defect cluster, respectively.

The specific hardness data and  $\sqrt{Nd}$  values of the studied alloys are given in Table 3. The  $\sqrt{Nd}$  values present the same variation trend as  $\Delta H$  with the increase in Cr content. The result confirms an agreement between macroscopic mechanical properties and micro defect statistics bridged by the theoretical model. In summary, the AlNbTiVCr exhibited relatively large irradiation-induced hardening due to the high density of dislocation loops. The reduced hardening in the other studied alloys compared with AlNbTiVCr also resembles the hardening transition from low-temperature ir-



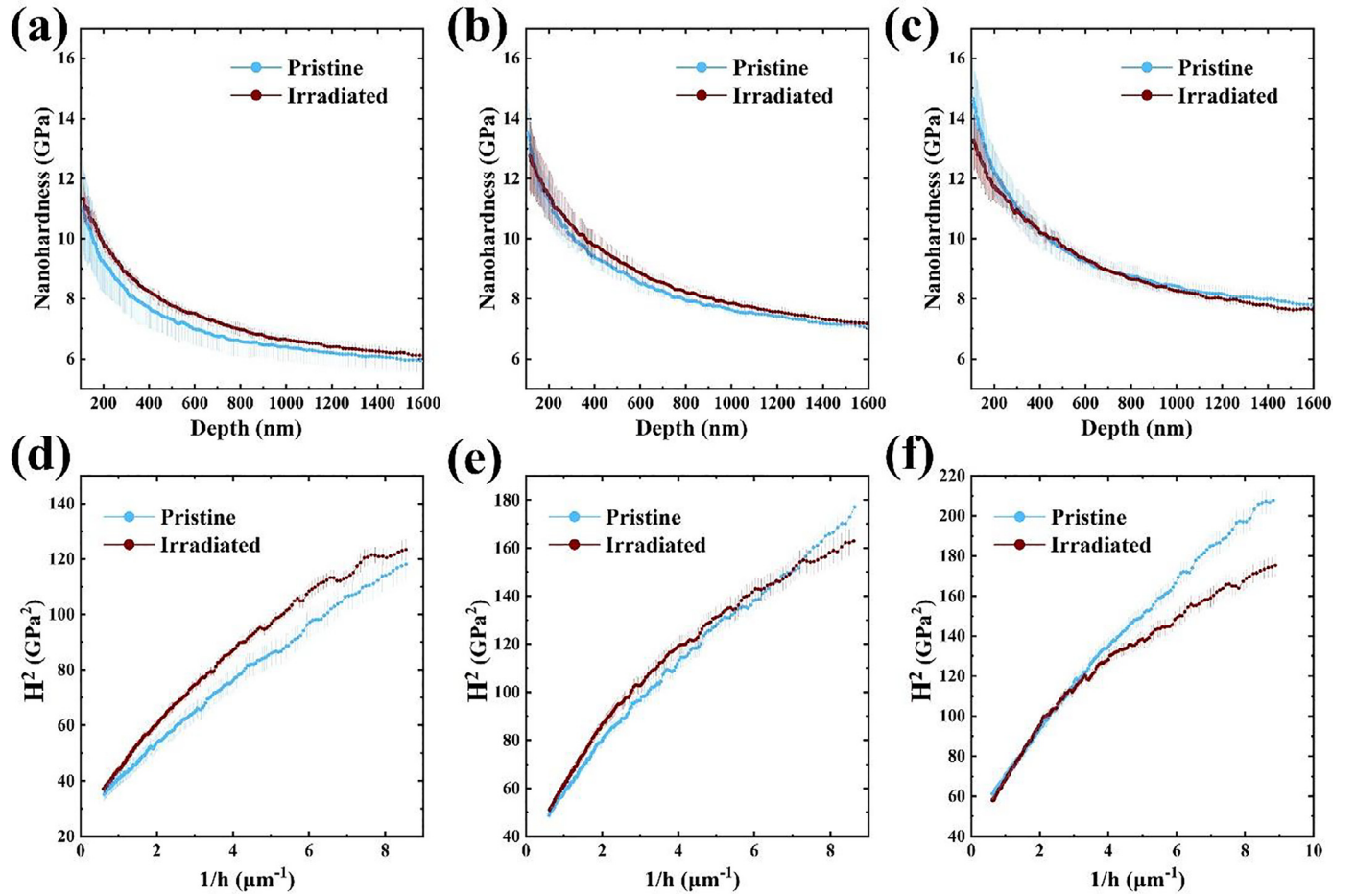


Fig. 7. Average nanoindentation hardness versus the indentation depth of the pristine and irradiated (a) AlNbTiV, (b) AlNbTiVCr<sub>0.5</sub>, and (c) AlNbTiVCr alloys. Square of the hardness ( $H^2$ ) versus the reciprocal of the indentation depth ( $1/h$ ) in (d) AlNbTiV, (e) AlNbTiVCr<sub>0.5</sub>, and (f) AlNbTiVCr alloys.

Table 3

Nanoindentation hardness of the pristine ( $H_{\text{pri}}$ ) and irradiated ( $H_{\text{irr}}$ ) AlNbTiVCr<sub>x</sub> ( $x = 0, 0.5, 1$ ) alloys and the square root of the product of dislocation loop density and size.

Sample	$H_{\text{pri}}$ (GPa)	$H_{\text{irr}}$ (GPa)	$\Delta H$ (GPa)	$(\text{Nd})^{0.5}$ ( $10^7$ /m)	$\Delta H/H_{\text{pri}}$
AlNbTiV	5.59	6.48	0.89	1.05	16%
AlNbTiVCr <sub>0.5</sub>	6.75	7.71	0.96	1.29	14%
AlNbTiVCr	7.38	8.91	1.53	1.72	21%

radiation to high-temperature irradiation [46]. Note that the hardening ratio ( $\Delta H/H_{\text{pri}}$ ) of AlNbTiVCr<sub>0.5</sub> is the lowest among the three alloys; it is lower than the Fe-Ni-Mn-Cr HEA irradiated at 500 °C to 1 dpa with the value of 18% and approaches to 0.3 dpa with the value of 10%–15%.

#### 4. Discussion

Lattice distortion, which essentially originates from the atomic size mismatch in an alloy, constitutes one of the main features distinguishing HEAs from other metallic materials [34,51]. The AlNbTiV has large lattice distortion. Because its  $\alpha_2$  parameter (= 0.072) is higher than most values of the solid solutions reported in a previous analysis of lattice distortion [52]. The first-principles calculation and  $\delta_{\text{INN}}$  parameter present here indicate an aggravated lattice distortion effect through the introduction of Cr. This finding may attribute to the lattice instability of Cr originates from its high DOS value, which require large relaxation distance to stabilize the lattice. This fact will modify the defect energy landscape. Intersti-

tials prefer to combine with Cr to reduce the energy of the system. The introduction of Cr represents the minimum of the energy landscapes. The aggravated lattice distortion and roughed energy landscapes affects the irradiation response of the AlNbTiVCr<sub>x</sub> system in the following aspects:

In the early stage of the irradiation, the severe lattice distortion can effectively decrease the electron mean free path and enhance phonon scattering in the early stage of irradiation [7]. Both contribute to slowing down the dissipation of the deposited heat, accelerating the recombination of defects and disfavoring void formation [53]. Thus, no void was found in the studied alloys irradiated at 600°C. In addition, the phase stability against irradiation may also be attributed to the lattice distortion effect as depicted in Section 3.3.

In the relaxation stage, the diffusion of self-interstitials in a rough energy landscape is like traversing rugged terrain, requiring frequent change in direction to seek the minimum migration energy path [53]. Now the calculation results of dumbbell interstitial composition and formation energy confirm Cr as the minimum

of the rugged energy landscapes. Thus, they interrupted the long-distance migration of self-interstitials, and the evolution of dislocation loops is delayed as the Cr content increases.

Nuclear materials are generally used in a temperature window range, in which degradation of mechanical properties induced by various deleterious effects is acceptable [45,54]. In the AlNbTiVCr<sub>x</sub> system, defect diffusion and dislocation growth are affected by local lattice distortion and energy landscapes, which is strongly correlated with Cr content. AlNbTiVCr<sub>0.5</sub> irradiated at high temperature did not form voids or precipitates like conventional alloys, nor did it produce high-density dislocation like AlNbTiVCr. Thus, the serious hardening or volume swelling at a certain high irradiation temperature can be avoided through composition regulating, which substantially extends the potential applications of HEAs in advanced nuclear energy systems.

## 5. Conclusion

First-principles calculation and ion irradiation experiments were used to reveal the lattice distortion and defect evolution of Al-Nb-Ti-V-Cr<sub>x</sub> ( $x = 0, 0.5, 1$ ) alloy system to explore the potential application of low-density RHEAs in advanced nuclear energy systems. Calculation results shows that Cr plays a crucial role as aggravating the lattice distortion and roughening the energy landscapes, thereby interrupted the long-distance migration of self-interstitials to delay their accumulation and long-distance migration. It is confirmed by the TEM results, which presents as the dislocation size monotonically decreases, and the density monotonically increases with the increasing Cr content in AlNbTiVCr<sub>x</sub> system.

Overall, the AlNbTiVCr present smaller loop size and AlNbTiVCr<sub>0.5</sub> exhibited lower irradiation hardening than the 316L stainless steel and 3d-transition metal HEAs under similar irradiation conditions. Compositional complexity exerts a remarkable impact on microstructural evolution in irradiated HEAs at elevated temperatures. This work provides an approach for better understanding the irradiation behavior of refractory HEAs and obtaining high-performance HEAs in irradiation tolerance efficiently.

## Declaration of competing interest

The authors declare that they have no known competing financial interests or personal relationships that could have appeared to influence the work reported in this paper.

## CRediT authorship contribution statement

**Guojia Ge:** Conceptualization, Methodology, Software, Validation, Formal analysis, Investigation, Data curation, Writing – original draft, Writing – review & editing. **Feida Chen:** Conceptualization, Writing – original draft, Writing – review & editing, Funding acquisition. **Xiaobin Tang:** Writing – original draft, Supervision, Project administration, Funding acquisition. **Yibo Wang:** Methodology, Software, Writing – original draft. **Changyuan Li:** Investigation, Writing – original draft.

## Acknowledgements

The authors would like to thank the Institute of Modern Physics (CAS) for providing irradiation experiment. Special thanks to Senior Engineer Niu of Suzhou Institute of Nano-Tech and Nano-Bionics (CAS) for his help in TEM characterization. In addition, this work was supported by China Postdoctoral Science Foundation (Grant

No. 2020M671488), the Fundamental Research Funds for the Central Universities (Grant No. NS2021036) and the Postgraduate Research & Practice Innovation Program of Jiangsu Province (Grant No. KYCX20\_0196).

## References

- [1] D.B. Miracle, O.N. Senkov, A critical review of high entropy alloys and related concepts, *Acta Mater* 122 (2017) 448–511, doi:10.1016/j.actamat.2016.08.081.
- [2] J.W. Yeh, S.K. Chen, S.J. Lin, J.Y. Gan, T.S. Chin, T.T. Shun, C.H. Tsau, S.Y. Chang, Nanostructured high-entropy alloys with multiple principal elements: Novel alloy design concepts and outcomes, *Adv. Eng. Mater.* 6 (2004) 299–303 +274, doi:10.1002/adem.200300567.
- [3] C. Lu, L. Niu, N. Chen, K. Jin, T. Yang, P. Xiu, Y. Zhang, F. Gao, H. Bei, S. Shi, M.R. He, I.M. Robertson, W.J. Weber, L. Wang, Enhancing radiation tolerance by controlling defect mobility and migration pathways in multicomponent single-phase alloys, *Nat. Commun.* 7 (2016) 1–8, doi:10.1038/ncomms13564.
- [4] K. Jin, H. Bei, Single-phase concentrated solid-solution alloys: bridging intrinsic transport properties and irradiation resistance, *Front. Mater.* 5 (2018) 1–11, doi:10.3389/fmats.2018.00026.
- [5] D.S. Aidhy, C. Lu, K. Jin, H. Bei, Y. Zhang, L. Wang, W.J. Weber, Point defect evolution in Ni, NiFe and NiCr alloys from atomistic simulations and irradiation experiments, *Acta Mater* 99 (2015) 69–76, doi:10.1016/j.actamat.2015.08.007.
- [6] S. Shen, F. Chen, X. Tang, G. Ge, J. Gao, Z. Sun, Irradiation damage and swelling of carbon-doped Fe38Mn40Ni11Al4Cr7 high-entropy alloys under heavy ion irradiation at elevated temperature, *J. Mater. Sci.* 55 (2020) 17218–17231, doi:10.1007/s10853-020-05229-7.
- [7] Y. Zhang, G.M. Stocks, K. Jin, C. Lu, H. Bei, B.C. Sales, L. Wang, L.K. B  land, R.E. Stoller, G.D. Samolyuk, M. Caro, A. Caro, W.J. Weber, Influence of chemical disorder on energy dissipation and defect evolution in concentrated solid solution alloys, *Nat. Commun.* 6 (2015), doi:10.1038/ncomms9736.
- [8] P. Yvon, F. Carr  , Structural materials challenges for advanced reactor systems, *J. Nucl. Mater.* 385 (2009) 217–222, doi:10.1016/j.jnucmat.2008.11.026.
- [9] K.L. Murty, I. Charit, Structural materials for Gen-IV nuclear reactors: challenges and opportunities, *J. Nucl. Mater.* 383 (2008) 189–195, doi:10.1016/j.jnucmat.2008.08.044.
- [10] Y. Lu, H. Huang, X. Gao, C. Ren, J. Gao, H. Zhang, S. Zheng, Q. Jin, Y. Zhao, C. Lu, T. Wang, T. Li, A promising new class of irradiation tolerant materials: Ti22ZrHfV0.5Mo0.2 high-entropy alloy, *J. Mater. Sci. Technol.* 35 (2019) 369–373, doi:10.1016/j.jmst.2018.09.034.
- [11] O. El-Atwani, N. Li, M. Li, A. Devaraj, J.K.S. Baldwin, M.M. Schneider, D. Sobieraj, J.S. Wr  bel, D. Nguyen-Manh, S.A. Maloy, E. Martinez, Outstanding radiation resistance of tungsten-based high-entropy alloys, *Sci. Adv.* 5 (2019) 1–10, doi:10.1126/sciadv.aav2002.
- [12] Y. Shi, B. Yang, P.K. Liaw, Corrosion-resistant high-entropy alloys: a review, *Metals (Basel)* 7 (2017) 1–18, doi:10.3390/met7020043.
- [13] N.D. Stepanov, N.Y. Yurchenko, D.G. Shaysultanov, G.A. Salishchev, M.A. Tikhonovsky, Effect of Al on structure and mechanical properties of AlxNbTiVzr ( $x=0, 0.5, 1, 1.5$ ) high entropy alloys, *Mater. Sci. Technol.* 31 (2015) 1184–1193, doi:10.1179/1743284715Y.00000000032.
- [14] O.N. Senkov, C. Woodward, D.B. Miracle, Microstructure and properties of aluminum-containing refractory high-entropy alloys, *JOM* 66 (2014) 2030–2042, doi:10.1007/s11837-014-1066-0.
- [15] O.N. Senkov, S.V. Senkova, C. Woodward, D.B. Miracle, Low-density, refractory multi-principal element alloys of the Cr-Nb-Ti-V-Zr system: microstructure and phase analysis, *Acta Mater* 61 (2013) 1545–1557, doi:10.1016/j.actamat.2012.11.032.
- [16] N.D. Stepanov, D.G. Shaysultanov, G.A. Salishchev, M.A. Tikhonovsky, Structure and mechanical properties of a light-weight AlNbTiV high entropy alloy, *Mater. Lett.* 142 (2015) 153–155, doi:10.1016/j.matlet.2014.11.162.
- [17] N.D. Stepanov, N.Y. Yurchenko, D.V. Skibin, M.A. Tikhonovsky, G.A. Salishchev, Structure and mechanical properties of the AlCrNbTiV ( $x = 0, 0.5, 1, 1.5$ ) high entropy alloys, *J. Alloys Compd.* 652 (2015) 266–280, doi:10.1016/j.jallcom.2015.08.224.
- [18] Z. Yao, M. Hernandez-Mayoral, M.L. Jenkins, M.A. Kirk, Heavy-ion irradiations of Fe and Fe-Cr model alloys Part 1: damage evolution in thin-foils at lower doses, 2008. <https://doi.org/10.1080/14786430802380469>.
- [19] K. Arakawa, M. Hatanaka, H. Mori, K. Ono, Effects of chromium on the one-dimensional motion of interstitial-type dislocation loops in iron, *J. Nucl. Mater.* 329–333 (2004) 1194–1198, doi:10.1016/j.jnucmat.2004.04.263.
- [20] D. Terentyev, G. Bonny, C. Domain, G. Monnet, L. Malerba, Mechanisms of radiation strengthening in Fe-Cr alloys as revealed by atomistic studies, *J. Nucl. Mater.* 442 (2013) 470–485, doi:10.1016/j.jnucmat.2013.03.054.
- [21] N. Scott Weingarten, E.F.C. Byrd, Special quasirandom structures of alon, *Comput. Mater. Sci.* 96 (2015) 312–318, doi:10.1016/j.commatsci.2014.09.021.
- [22] A. Van De Walle, P. Tiwary, M. De Jong, D.L. Olmsted, M. Asta, A. Dick, D. Shin, Y. Wang, L.Q. Chen, Z.K. Liu, Efficient stochastic generation of special quasirandom structures, *Calphad Comput. Coupling Phase Diagrams Thermochem.* 42 (2013) 13–18, doi:10.1016/j.calphad.2013.06.006.
- [23] C. Niu, C.R. LaRosa, J. Miao, M.J. Mills, M. Ghazisaeidi, Magnetically-driven phase transformation strengthening in high entropy alloys, *Nat. Commun.* 9 (2018) 1–9, doi:10.1038/s41467-018-03846-0.
- [24] J.P. Perdew, K. Burke, M. Ernzerhof, Generalized gradient approximation made simple, *Phys. Rev. Lett.* 77 (1996) 3865–3868, doi:10.1103/PhysRevLett.77.3865.



- [25] G. Kresse, J. Furthmüller, Efficiency of ab-initio total energy calculations for metals and semiconductors using a plane-wave basis set, *Comput. Mater. Sci.* 6 (1996) 15–50, doi:[10.1016/0927-0256\(96\)00008-0](https://doi.org/10.1016/0927-0256(96)00008-0).
- [26] G. Kresse, J. Furthmüller, Efficient iterative schemes for ab initio total-energy calculations using a plane-wave basis set, *Phys. Rev. B* 54 (1996) 11169–11186, doi:[10.1103/PhysRevB.54.11169](https://doi.org/10.1103/PhysRevB.54.11169).
- [27] T.P.C. Klaver, D.J. Hepburn, G.J. Ackland, Defect and solute properties in dilute Fe–Cr–Ni austenitic alloys from first principles, *Phys. Rev. B* 85 (2012) 174111, doi:[10.1103/PhysRevB.85.174111](https://doi.org/10.1103/PhysRevB.85.174111).
- [28] S. Zhao, G.M. Stocks, Y. Zhang, Defect energetics of concentrated solid-solution alloys from ab initio calculations: Ni<sub>0.5</sub>Co<sub>0.5</sub>, Ni<sub>0.5</sub>Fe<sub>0.5</sub>, Ni<sub>0.8</sub>Fe<sub>0.2</sub> and Ni<sub>0.8</sub>Cr<sub>0.2</sub>, *Phys. Chem. Chem. Phys.* 18 (2016) 24043–24056, doi:[10.1039/C6CP05161H](https://doi.org/10.1039/C6CP05161H).
- [29] B. Wldom, Some topics in the theory of fluids, *J. Chem. Phys.* 39 (1963) 2808–2812, doi:[10.1063/1.1734110](https://doi.org/10.1063/1.1734110).
- [30] R.E. Stoller, M.B. Toloczko, G.S. Was, A.G. Certain, S. Dwaraknath, F.A. Garner, On the use of SRIM for computing radiation damage exposure, *Nucl. Instruments Methods Phys. Res. Sect. B Beam Interact. with Mater. Atoms* 310 (2013) 75–80, doi:[10.1016/j.nimb.2013.05.008](https://doi.org/10.1016/j.nimb.2013.05.008).
- [31] W.C. Oliver, G.M. Pharr, An improved technique for determining hardness and elastic modulus using load and displacement sensing indentation experiments, *J. Mater. Res.* 7 (1992) 1564–1583, doi:[10.1557/JMR.1992.1564](https://doi.org/10.1557/JMR.1992.1564).
- [32] W.D. Nix, H. Gao, Indentation size effects in crystalline materials: A law for strain gradient plasticity, *J. Mech. Phys. Solids* 46 (1998) 411–425, doi:[10.1016/S0022-5096\(97\)00086-0](https://doi.org/10.1016/S0022-5096(97)00086-0).
- [33] R. Kasada, Y. Takayama, K. Yabuuchi, A. Kimura, A new approach to evaluate irradiation hardening of ion-irradiated ferritic alloys by nano-indentation techniques, *Fusion Eng. Des.* 86 (2011) 2658–2661, doi:[10.1016/j.fusengdes.2011.03.073](https://doi.org/10.1016/j.fusengdes.2011.03.073).
- [34] C. Lee, G. Song, M.C. Gao, R. Feng, P. Chen, J. Brechtel, Y. Chen, K. An, W. Guo, J.D. Poplawsky, S. Li, A.T. Samaei, W. Chen, A. Hu, H. Choo, P.K. Liaw, Lattice distortion in a strong and ductile refractory high-entropy alloy, *Acta Mater* 160 (2018) 158–172, doi:[10.1016/j.actamat.2018.08.053](https://doi.org/10.1016/j.actamat.2018.08.053).
- [35] S. Zhao, Defect properties in a VTaCrW equiatomic high entropy alloy (HEA) with the body centered cubic (bcc) structure, *J. Mater. Sci. Technol.* 44 (2020) 133–139, doi:[10.1016/j.jmst.2019.10.025](https://doi.org/10.1016/j.jmst.2019.10.025).
- [36] S. Zhao, Y. Ossetsky, Y. Zhang, Preferential diffusion in concentrated solid solution alloys: NiFe, NiCo and NiCoCr, *Acta Mater* 128 (2017) 391–399, doi:[10.1016/j.actamat.2017.01.056](https://doi.org/10.1016/j.actamat.2017.01.056).
- [37] A. Barashev, Y. Ossetsky, H. Bei, C. Lu, L. Wang, Y. Zhang, Chemically-biased diffusion and segregation impede void growth in irradiated Ni-Fe alloys, *Curr. Opin. Solid State Mater. Sci.* 23 (2019) 92–100, doi:[10.1016/j.cossms.2018.12.001](https://doi.org/10.1016/j.cossms.2018.12.001).
- [38] X.K. Zhang, J.C. Huang, P.H. Lin, T.Y. Liu, Y.C. Wu, W.P. Li, Y.N. Wang, Y.C. Liao, J.S.C. Jang, Microstructure and mechanical properties of Tix(AlCrVNb)100-x light weight multi-principal element alloys, *J. Alloys Compd.* 831 (2020), doi:[10.1016/j.jallcom.2020.154742](https://doi.org/10.1016/j.jallcom.2020.154742).
- [39] I.L.W. Wilson, M.G. Burke, The effect of microstructure on the SCC behavior of alloy 718, *Superalloys 718, 625 Var, Deriv* (1991) 681–693.
- [40] T. Nagase, P.D. Rack, J.H. Noh, T. Egami, In-situ TEM observation of structural changes in nano-crystalline CoCrCuFeNi multicomponent high-entropy alloy (HEA) under fast electron irradiation by high voltage electron microscopy (HVEM), *Intermetallics* 59 (2015) 32–42, doi:[10.1016/j.intermet.2014.12.007](https://doi.org/10.1016/j.intermet.2014.12.007).
- [41] G. Ge, F. Chen, X. Tang, C. Li, J. Gao, S. Li, Z. Geng, Effects of order and disorder on the defect evolution of NiFe binary alloys from atomistic simulations, *Nucl. Instruments Methods Phys. Res. Sect. B Beam Interact. with Mater. Atoms* 498 (2021) 27–33, doi:[10.1016/j.nimb.2021.04.012](https://doi.org/10.1016/j.nimb.2021.04.012).
- [42] J.A. Hudson, Void formation in solution-treated aisi 316 and 321 stainless steels under 46.5 mev ni<sup>6+</sup> irradiation, *J. Nucl. Mater.* 60 (1976) 89–106, doi:[10.1016/0022-3115\(76\)90121-5](https://doi.org/10.1016/0022-3115(76)90121-5).
- [43] T.M. Williams, Interstitial loop nucleation and growth in solution-treated type 316 stainless steel irradiated to low doses with 22 MeV C<sup>2+</sup> and 46.5 MeV Ni<sup>6+</sup> ions, *J. Nucl. Mater.* 79 (1979) 28–42, doi:[10.1016/0022-3115\(79\)90431-8](https://doi.org/10.1016/0022-3115(79)90431-8).
- [44] J. Gan, E.P. Simonen, S.M. Bruemmer, L. Fournier, B.H. Sencer, G.S. Was, The effect of oversized solute additions on the microstructure of 316SS irradiated with 5 MeV Ni<sup>++</sup> ions or 3.2 MeV protons, *J. Nucl. Mater.* 325 (2004) 94–106, doi:[10.1016/j.jnucmat.2003.11.002](https://doi.org/10.1016/j.jnucmat.2003.11.002).
- [45] T. Yang, W. Guo, J.D. Poplawsky, D. Li, L. Wang, Y. Li, W. Hu, M.L. Crespiello, Z. Yan, Y. Zhang, Y. Wang, S.J. Zinkle, Structural damage and phase stability of Al<sub>0.3</sub>CoCrFeNi high entropy alloy under high temperature ion irradiation, *Acta Mater* 188 (2020) 1–15, doi:[10.1016/j.actamat.2020.01.060](https://doi.org/10.1016/j.actamat.2020.01.060).
- [46] N.A.P.K. Kumar, C. Li, K.J. Leonard, H. Bei, S.J. Zinkle, Microstructural stability and mechanical behavior of FeNiMnCr high entropy alloy under ion irradiation, *Acta Mater* 113 (2016) 230–244, doi:[10.1016/j.actamat.2016.05.007](https://doi.org/10.1016/j.actamat.2016.05.007).
- [47] H.F. Huang, J.J. Li, D.H. Li, R.D. Liu, G.H. Lei, Q. Huang, L. Yan, TEM, XRD and nanoindentation characterization of Xenon ion irradiation damage in austenitic stainless steels, *J. Nucl. Mater.* 454 (2014) 168–172, doi:[10.1016/j.jnucmat.2014.07.033](https://doi.org/10.1016/j.jnucmat.2014.07.033).
- [48] X. Liu, R. Wang, A. Ren, J. Jiang, C. Xu, P. Huang, W. Qian, Y. Wu, C. Zhang, Evaluation of radiation hardening in ion-irradiated Fe based alloys by nanoindentation, *J. Nucl. Mater.* 444 (2014) 1–6, doi:[10.1016/j.jnucmat.2013.09.026](https://doi.org/10.1016/j.jnucmat.2013.09.026).
- [49] S. Shen, F. Chen, X. Tang, J. Lin, G. Ge, J. Liu, Effects of carbon doping on irradiation resistance of Fe<sub>38</sub>Mn<sub>40</sub>Ni<sub>11</sub>Al<sub>4</sub>Cr<sub>7</sub> high entropy alloys, *J. Nucl. Mater.* 540 (2020) 152380, doi:[10.1016/j.jnucmat.2020.152380](https://doi.org/10.1016/j.jnucmat.2020.152380).
- [50] J.S. Benjamin, M.J. Bomford, Dispersion strengthened aluminum made by mechanical alloying, *Metall. Trans. A* 8 (1977) 1301–1305, doi:[10.1007/BF02643845](https://doi.org/10.1007/BF02643845).
- [51] Y. Zhang, T.T. Zuo, Z. Tang, M.C. Gao, K.A. Dahmen, P.K. Liaw, Z.P. Lu, Microstructures and properties of high-entropy alloys, *Prog. Mater. Sci.* 61 (2014) 1–93, doi:[10.1016/j.pmatsci.2013.10.001](https://doi.org/10.1016/j.pmatsci.2013.10.001).
- [52] Z. Wang, W. Qiu, Y. Yang, C.T. Liu, Atomic-size and lattice-distortion effects in newly developed high-entropy alloys with multiple principal elements, *Intermetallics* 64 (2015) 63–69, doi:[10.1016/j.intermet.2015.04.014](https://doi.org/10.1016/j.intermet.2015.04.014).
- [53] Z. Su, J. Ding, M. Song, L. Jiang, T. Shi, Z. Li, S. Wang, F. Gao, D. Yun, C. Lu, Radiation-tolerant high-entropy alloys via interstitial-solute-induced chemical heterogeneities, *ArXiv Prepr. ArXiv2103.15134*. (2021).
- [54] S.J. Zinkle, N.M. Ghoniem, Operating temperature windows for fusion reactor structural materials, *Fusion Eng. Des.* 51 (2000) 55–71, doi:[10.1016/S0920-3796\(00\)00320-3](https://doi.org/10.1016/S0920-3796(00)00320-3).